

This is an Open Access document downloaded from ORCA, Cardiff University's institutional repository: <https://orca.cardiff.ac.uk/id/eprint/128239/>

This is the author's version of a work that was submitted to / accepted for publication.

Citation for final published version:

Yang, Zihao, Zhang, Yongcun, Liu, Shutian and Wu, Zhangming 2021. Design and analysis of dual-constituent lattice sandwich panel with in-plane zero thermal expansion and high structural stiffness. *Mechanics of Advanced Materials and Structures* 28 (17) , pp. 1743-1754. 10.1080/15376494.2019.1704099

Publishers page: <http://dx.doi.org/10.1080/15376494.2019.1704099>

Please note:

Changes made as a result of publishing processes such as copy-editing, formatting and page numbers may not be reflected in this version. For the definitive version of this publication, please refer to the published source. You are advised to consult the publisher's version if you wish to cite this paper.

This version is being made available in accordance with publisher policies. See <http://orca.cf.ac.uk/policies.html> for usage policies. Copyright and moral rights for publications made available in ORCA are retained by the copyright holders.



Design and analysis of dual-constituent lattice sandwich panel with in-plane zero thermal expansion and high structural stiffness

Zihao Yang^a, Yongcun Zhang^{a,*}, Shutian Liu^a, Zhangming Wu^b

^a State Key Laboratory of Structural Analysis for Industrial Equipment, Dalian University of Technology, Dalian, 116024, China

^b Cardiff School of Engineering, Queens Buildings, The Parade, Newport Road, Cardiff CF24 3AA, UK

Corresponding author: yczhang@dlut.edu.cn

Abstract: The lattice sandwich panel may achieve in-plane zero thermal expansion (ZTE) property through a special design of upper and lower face sheets, both of which are attached with an additional layer of patch with high coefficient of thermal expansion (CTE). This type of sandwich panels with ZTE property is highly demanded for aerospace vehicles, where often suffer from large variations of temperature. The design of curved surface for the face sheet cells is necessary to achieve in-plane ZTE attribute, however, it will also result in structural stiffness reduction significantly. In this study, a novel dual-constituent lattice sandwich panel with in-plane ZTE and high structural stiffness properties is proposed, designed and analyzed. Six different kinds of cell configurations through two types of curved surface and three different patches are compared to obtain the optimal design. A further parametric study is carried out by numerical simulations to show the influences of curved surface, patch covering form, patch shape, size and thickness on cell equivalent stiffness as well as the control effectiveness of thermal deformation. Optimal cell designs that enable the sandwich panels to achieve the in-plane ZTE and high in-plane stiffness properties are also presented. The stiffness reduction for achieving in-plane ZTE is acceptable. Sufficient residual stiffness ensures the load carrying capacity of dual-constituent lattice sandwich panels.

Keywords: Zero thermal expansion; Lattice structure; Sandwich panel; Multifunctional design; Metamaterial

1. Introduction

Lattice core sandwich panels have attracted extensive interests due to their inherent advantages of lightweight and excellent mechanical properties, and have been used in a broad range of applications in weight sensitive aerospace engineering. It is widely acknowledged that aerospace structures often experience large variations of temperature, which gives rise to extremely high thermal stress/deformation leading to structural failure. One example is that aerodynamic heating on the hypersonic vehicles during its flight results in excessively high local thermal stress and strain, which subsequently wreck the entire aerodynamic shapes [1, 2]. Another example is in the process of earth-orbiting satellites passing from sunlight to shade, repeatedly. In this example, significant temperature changes generate undesirable thermal deformation, which

deteriorates the working space of on-board instruments. Consequently it leads to the loss of precision for sensitive optical telescopes [3, 4]. Therefore, it is desirable to develop advanced structures with ultralow (ideally zero) thermal expansion attribution.

One direct method is to manufacture the lattice sandwich panels using natural bulk materials with low or zero CTEs. However, the inherent defects such as narrow control range of ZTE and poor mechanical performance limit their practice applications. For example, Invar is a robust material, but exhibits low thermal expansion attribute only between 0 and 100°C. Zerodur has low thermal expansion coefficient over a larger temperature range, however, it is a type of glass ceramic that is not appropriately used for reliable load carrying structures. Fiber-reinforced [5] or particulate-reinforced [6] composites can achieve near-zero CTEs through embedding fibers or particulates of materials with negatives CTEs [7]. However, very few known materials in forms of practices that possess negative CTE can be used as reinforcements. Furthermore, great difference on CTEs between the fiber (or particulate) and the matrix may cause interface cracking on heating, which inevitably leads to the delamination failure.

Metamaterials, or artificial materials with well-designed constituents of two different positive CTEs and void space are an alternative way to achieve ZTE attribute and high stiffness properties, simultaneously. A number of notable design concepts of dual-constituent for metamaterials have been proposed by Lakes [8, 9], Sigmund and Torquato [10, 11], Steeves et al. [12, 13], Wei et al. [14, 15], Xu and Pasini [16, 17] and Zhang et al. [18, 19]. These material design concepts can be extended to the structural forms straightforwardly because there is no apparent size effect. For example, a range of lattice structures such as lattice face-sheets for sandwich panel [20], lattice cylindrical shells [21] and satellite support structures [22], are subsequently proposed based on the original mechanism developed from the lattice metamaterials. It is worth noting that the void space is necessary for combining two constituents with different CTEs to achieve the desired thermal behavior. Because of the existing of porous materials, these new-designed structures are unsuitable for the applications involving sealing, for example, the skin of supersonic vehicle [20] and containing space.

In order to meet the above demand, a new design concept of dual-constituent sandwich panel with in-plane ZTE was proposed in our previous works [23]. Different with the structures consisting of porous metamaterial that achieve ZTE attribute, the upper and lower face sheets of the newly designed sandwich panels are all solid with no porosity. The ultralow in-plane thermal deformation was verified by two different structural forms: corrugated and lattice sandwich panels. However, the analysis and the optimal stiffness design of their mechanical performance have not been explored. In this work, a novel dual-constituent lattice sandwich panel is designed and analyzed, in which the weight, the mechanical performance and functionality (in-plane ZTE) are considered, simultaneously. The paper is organized in the following manner: the whole

configuration for the new design of dual-constituent lattice sandwich panel is presented firstly in Section 2. Subsequently, the detailed design for the face sheet cell including the curved surface and patch configurations designs are presented in the rest of Section 2. The numerical methods that are developed to predict the cell CTEs and equivalent stiffness are presented in details in Section 3. The comprehensive evaluations on cell designs considering the efficiency of thermal deformation control and equivalent stiffness are conducted in Section 4. Finally, the conclusions are summarized in Section 5.

2. Structural design

As shown in Fig.1, the whole configuration of dual-constituent lattice sandwich panel with in-plane zero thermal expansion (ZTE) consists of upper and lower face sheets and a truss core. The counterintuitive properties of ultralow or near zero thermal expansion are attributed from the special design of face sheets, which are comprised of bi-layer materials with different positive coefficients of thermal expansion (CTEs) in each cell. Two bonded layers with different CTEs will give rise to transverse bending to the face sheet during the process of temperature increasing, which results in the in-plane contraction that can compensate the in-plane thermal expansion. One of the key designs to achieve the in-plane ZTE attribute for the lattice sandwich panel is that the bi-layer part of face sheets should be curved, which can enlarge the magnitude of thermal bending deformation.

The truss core provides the necessary support for the face sheets by connecting four corner points of every periodic cell. In doing so, the same transverse bending deformation is ensured in the local cell to prevent the possible overall transverse deformation of face sheets during the heating. The most attractive feature is that face sheets of the sandwich panels are all solid with no porosity, which can efficiently isolate the internal environment from the external harsh environment. Therefore, this new design of sandwich panels can be placed at the outermost of structures where the sealing is needed.

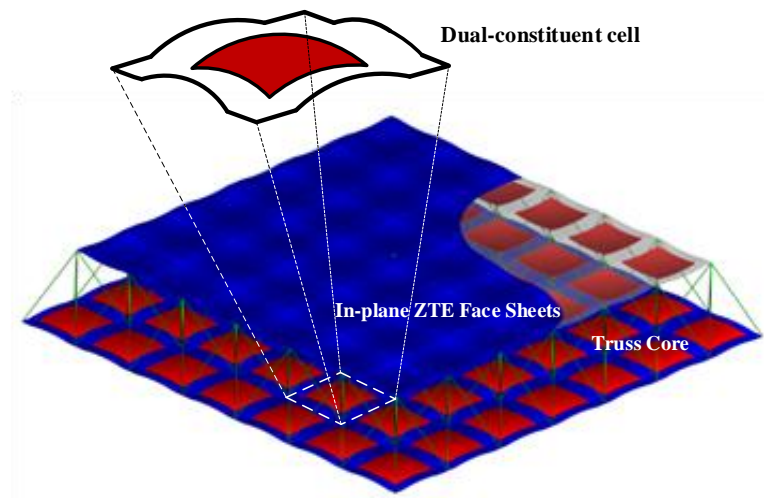


Fig.1. The whole configuration of dual-constituent lattice sandwich panel.

The curved surface of face sheet is necessary for generating enough curvature during the thermal expansion process, but the curved surface design will weaken the stiffness of sandwich panel, significantly. In addition, the configuration of the attached patches is another important design aspect on its stiffness and thermal expansion. In order to validate the design principles with above mentioned considerations, six face sheet cell designs through the combination of two different curved surfaces and three patch types are analyzed and compared.

Although the design of curved part is necessary for achieving the in-plane ZTE, it will cause the stiffness reduction, inevitably. Therefore, the design target that the face sheets possess both high stiffness and in-plane ZTE can be achieved through designing a little curvature for the curved part and a large region for the flat part. To this end, two different curved surfaces for the cell are designed herein. Their geometry and area configurations are shown in Fig.2(a) and (b), respectively.

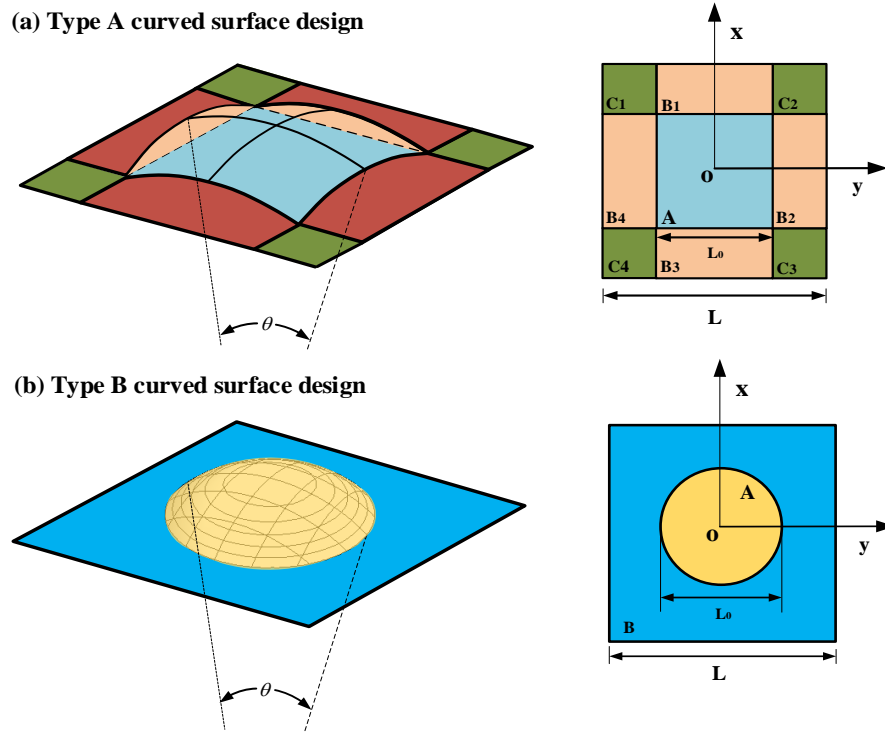


Fig.2. The geometry and area configurations of the two designs of curved surface of cell. (a) Type A curved surface. (b) Type B curved surface.

As shown in Fig.2, for both Types A and B, the central area A is the key part that can thermally trigger the mechanism of bending adjustment. For the Type A, the geometry of area A in

the curved surface can be expressed, mathematically, as follows:

$$\text{Area } A: \begin{cases} -\frac{L_0}{2} \leq x \leq \frac{L_0}{2} \\ -\frac{L_0}{2} \leq y \leq \frac{L_0}{2} \end{cases} \quad \sqrt{\rho^2 - x^2} + \sqrt{\rho^2 - y^2} - \rho - z = 0 \quad (1)$$

where L_0 and ρ are the side length and the curvature radius of the center area A , and θ is the curved surface angle. If the angle is small enough, the curvature radius ρ is simply reduced to L_0 / θ , and then the Eq.(1) is rewritten as:

$$\text{Area } A: \begin{cases} -\frac{L_0}{2} \leq x \leq \frac{L_0}{2} \\ -\frac{L_0}{2} \leq y \leq \frac{L_0}{2} \end{cases} \quad \sqrt{\left(\frac{L_0}{\theta}\right)^2 - x^2} + \sqrt{\left(\frac{L_0}{\theta}\right)^2 - y^2} - \frac{L_0}{\theta} - z = 0 \quad (2)$$

The surrounding area B represents the regions that are not covered by patches, and therefore will not be used for the control of the cell thermal deformation control. To improve the cell mechanical performance, the area B must be designed as flat as possible. The geometry of the area B is defined as:

$$\begin{aligned} \text{Area } B_1: & \begin{cases} -\frac{L}{2} \leq x \leq -\frac{L_0}{2} \\ -\frac{L_0}{2} \leq y \leq \frac{L_0}{2} \end{cases} \quad \sqrt{\frac{L_0^2}{\theta^2} - \frac{L_0^2}{4}} + \sqrt{\frac{L_0^2}{\theta^2} - y^2} - \frac{L_0}{\theta} + \frac{(1+2x)(\sqrt{\frac{L_0^2}{\theta^2} - \frac{L_0^2}{4}} - \sqrt{\frac{L_0^2}{\theta^2} - y^2})}{1-L} - z = 0 \\ \text{Area } B_2: & \begin{cases} -\frac{L_0}{2} \leq x \leq \frac{L_0}{2} \\ -\frac{L_0}{2} \leq y \leq -\frac{L}{2} \end{cases} \quad \sqrt{\frac{L_0^2}{\theta^2} - \frac{L_0^2}{4}} + \sqrt{\frac{L_0^2}{\theta^2} - x^2} - \frac{L_0}{\theta} + \frac{(1+2y)(\sqrt{\frac{L_0^2}{\theta^2} - \frac{L_0^2}{4}} - \sqrt{\frac{L_0^2}{\theta^2} - x^2})}{1-L} - z = 0 \\ \text{Area } B_3: & \begin{cases} \frac{L_0}{2} \leq x \leq \frac{L}{2} \\ -\frac{L_0}{2} \leq y \leq \frac{L_0}{2} \end{cases} \quad \sqrt{\frac{L_0^2}{\theta^2} - \frac{L_0^2}{4}} + \sqrt{\frac{L_0^2}{\theta^2} - y^2} - \frac{L_0}{\theta} + \frac{(1-2x)(\sqrt{\frac{L_0^2}{\theta^2} - \frac{L_0^2}{4}} - \sqrt{\frac{L_0^2}{\theta^2} - y^2})}{1-L} - z = 0 \\ \text{Area } B_4: & \begin{cases} -\frac{L_0}{2} \leq x \leq \frac{L_0}{2} \\ \frac{L_0}{2} \leq y \leq \frac{L}{2} \end{cases} \quad \sqrt{\frac{L_0^2}{\theta^2} - \frac{L_0^2}{4}} + \sqrt{\frac{L_0^2}{\theta^2} - x^2} - \frac{L_0}{\theta} + \frac{(1-2y)(\sqrt{\frac{L_0^2}{\theta^2} - \frac{L_0^2}{4}} - \sqrt{\frac{L_0^2}{\theta^2} - x^2})}{1-L} - z = 0 \end{aligned} \quad (3)$$

The areas C in the Type A curved surface are completely flat and only contain single-constituent materials, and are expressed as,

$$\text{Area } C: \begin{cases} -\frac{L}{2} \leq x \leq -\frac{L_0}{2}, \frac{L_0}{2} \leq x \leq \frac{L}{2} \\ -\frac{L}{2} \leq y \leq -\frac{L_0}{2}, \frac{L_0}{2} \leq y \leq \frac{L}{2} \end{cases} \quad \sqrt{4L_0^2 - L^2} - \frac{L_0}{\theta} - z = 0 \quad (4)$$

The other design of Type B curved surface includes only a centrally spherical area that is

designed to meet the requirement of bi-directional initial curvatures for the cell thermal deformation control. Compared with the Type A curved surface, this new curved surface B design is more concise, and likely exhibit high stiffness properties because there is no redundant single-constituent curved part. The geometry of Type B curved surface is defined as follows:

$$\begin{aligned} \text{Area A: } & x^2 + y^2 \leq \frac{L_0^2}{4} \quad x^2 + y^2 + z^2 - \frac{L_0^2}{\theta^2} = 0 \\ \text{Area B: } & \begin{cases} -\frac{L}{2} \leq x \leq \frac{L}{2}, -\frac{L}{2} \leq y \leq \frac{L}{2} \\ x^2 + y^2 > \frac{L_0^2}{4} \end{cases} \quad \sqrt{\frac{L_0^2(4-\theta^2)}{4\theta^2}} - z = 0 \end{aligned} \quad (5)$$

Subsequently, three different patch shapes which are square, circle and cross are designed to cover both the types A and B curved surfaces. Therefore, six different cell types for the face sheets are designed and illustrated in Fig.3 (a-f) in terms of the defined geometric parameters. In order to control the number of design variables, the patch and the curved surface are both assumed to be doubly symmetric. The side length of cross-shaped patch is fixed to be $L_0/2$ and thus the sole in-plane design parameter L_0 that is used to adjust the patch areas of each cell is determined. Furthermore, the volume ratio V_0/V of the patch to curved surface is another design parameter considering the structural thicknesses. The volumes V_0 and V can be approximately evaluated by the products of the projected area and the thickness if the curved angle θ is sufficiently small. The formulas for evaluating the volume ratio V_0/V for each type of cell designs are given as follows:

$$\begin{aligned} \text{Cell(a)} \quad V_0/V &= \frac{L_0^2 t_0}{L^2 t} & \text{Cell(b)} \quad V_0/V &= \frac{\pi L_0^2 t_0}{4L^2 t} & \text{Cell(c)} \quad V_0/V &= \frac{3L_0^2 t_0}{4L^2 t} \\ \text{Cell(d)} \quad V_0/V &= \frac{L_0^2 t_0}{2L^2 t} & \text{Cell(e)} \quad V_0/V &= \frac{\pi L_0^2 t_0}{4L^2 t} & \text{Cell(f)} \quad V_0/V &= \frac{(\pi - 2 + \sqrt{3})L_0^2 t_0}{4L^2 t} \end{aligned} \quad (6)$$

where t_0 and t are the thicknesses of the patch and the curved surface, respectively.

The process for cell evaluations and parameter investigations can be divided into the following three phases:

- (I) The evaluation on curved surface designs is performed, firstly, through comparing the cells with the same patch shape. As a representative example, a pair of cells (a) and (d) is firstly selected, and cell (e) is also added for further verification. The evaluation is mainly focused on the control efficiency of thermal deformation, i.e., the difficulty of achieving the in-plane ZTE attribute.

- (II) According to the results obtained in the first phase, a curved surface type with the best performance is used as the basis for the comparison of stiffness properties. During this phase, the cells (a)-(c) or (d)-(g) with the same curved surface type but different patch shapes are selected for the evaluation.
- (III) After the completion of phases (I) and (II), it will be straightforward to determine the best cell design among the six types of cells. The further design of patch thickness to improve the stiffness properties will be considered afterwards.

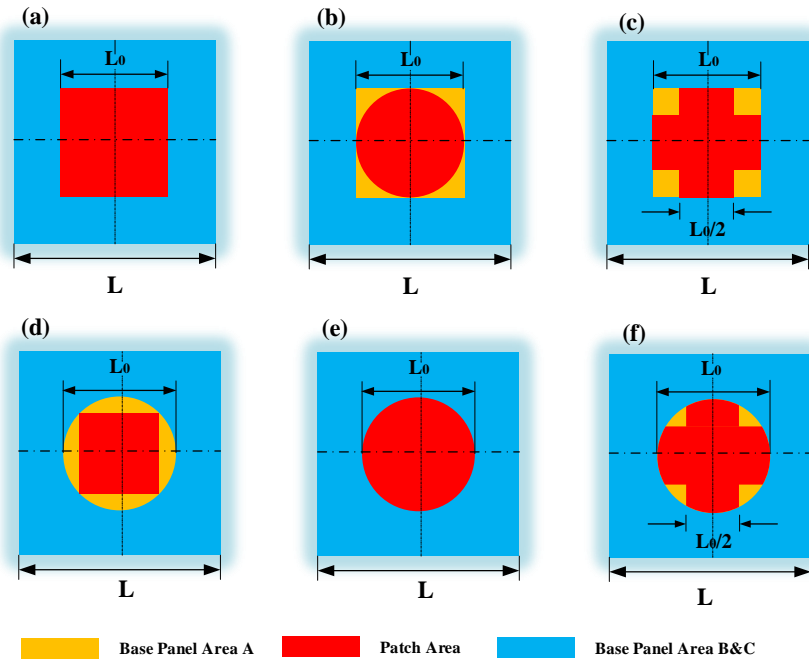


Fig.3. The six designs of cell of face sheet combining two types of curved surfaces. (a)-(c) The cells with sharing Type A curved surface. (d)-(f) The cells with sharing Type B curved surface.

The cell geometric parameters are listed in Table 1. The values of curved angle θ is set to be less than $\pi/30$ (6°). In fact, a very large value θ will significantly weaken the cell in-plane stiffness, whereas an excessively small θ will be unable to trigger the thermal bending-adjustment mechanism. With respect to the material selections, theoretically, it is possible to use any arbitrary two types of materials with different positive CTEs to achieve the in-plane ZTE. For instance, the commonly available alloy Invar is taken for the curved surfaces and the Aluminum alloy is used for the patches. The material properties of Invar and Aluminum alloy are listed in Table 2.

Table 1 The geometric sizes used in numerical simulation.

L/m	t_0/m	t/m	Range of θ
5×10^{-2}	5×10^{-4}	5×10^{-4}	$\leq \pi / 30$ (6°)

Table 2 The material properties [24] of Invar and Aluminum alloy used in numerical simulation.

Material member	Young's Modulus (GPa)	CTE α ($ppm / ^\circ C$)	Poisson's ratio ν	Density ρ (Kg / m^3)
Invar (Curved surface)	140	1.0	0.28	8100
Al 7075-T6 (Patch)	70	22.2	0.33	2800

3. Numerical analysis

3.1 Finite element analysis for thermal expansion

Due to the geometric complexities of the cell of face sheets with bi-directional curvature, it is difficult to obtain the analytical solutions of CTEs for the cell. Therefore, the finite element analysis (FEA) is conducted to verify the in-plane ZTE design objective for the dual-constituent lattice sandwich panel. The commercial software ANSYS 15.0 is used in this work to perform the finite element simulation. Since the shell element is appropriate for modeling the cells with large aspect ratio, the element type shell181 (in ANSYS) is adopted. In order to ensure the mesh quality and convergence, the models are meshed with a fine mesh size 8×10^{-4} . As a result, about 4000 elements are set for each model to ensure achieving convergent results. The boundary conditions applied to the cells during FE analysis process are shown in the Fig.4. Boundary condition (1): the x-displacement of side 1 and the y-displacement of side 2 are firstly restricted. While, the x-displacements of all nodes at side 3 are coupled together; the y-displacements of all nodes at side 4 are coupled together too. The intentions of the boundary condition (1) are to prevent rigid-body displacement in X-Y plane, and simultaneously promise the thermal deformations consistence at side 2 and 3. Boundary condition (2): the z-displacements of the nodes at four corner points are restricted. The intention of the boundary condition (2) is to prevent possible overall z-displacement on heating. Actually, this boundary condition replaces the effect of truss core on the cell. Boundary condition (3): the x-rotations of both side 1 and 3 and the y-rotations of both side 2 and 4 are finally restricted. The intention of the boundary condition (3) is to replace the influences of surrounding cells. Note, the thermal deformation along cell thickness direction is varied due to the bending, and thus the displacement of the neutral plane of curved surface is used

to calculate the effective CTEs. In order to directly determine the thermal deformation, the shell mid-surface is set at the middle of the cell curved surface.

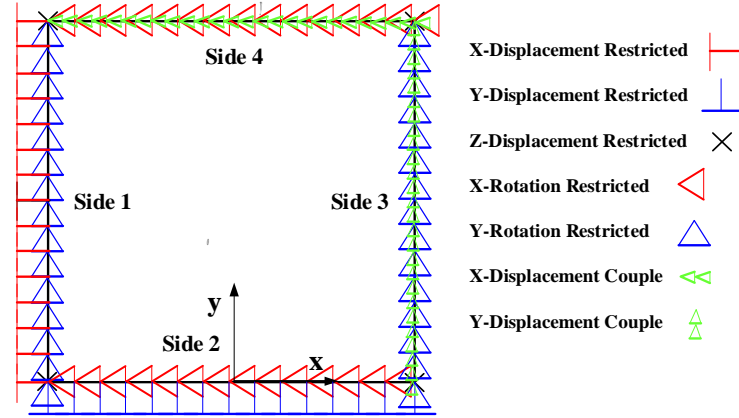


Fig.4. The boundary conditions applied to face sheet cell during FE analysis process.

3.2 Cell stiffness prediction based on Asymptotic Homogenization method

The equivalent stiffness of face sheet cell is another important index for assessing the mechanical performance of each cell that is designed to achieve the in-plane ZTE attribute. Since no analytical solution for cell stiffness is available, the Asymptotic Homogenization Theory with finite element implement (NIAH) [25] is adopted for analyzing the periodic inhomogeneous panel and shell structures. In this method, the equivalent generalized stiffness matrix for each cell is obtained by means of considering the FEA in ANSYS as a black box. The whole procedure of NIAH for the cell stiffness prediction is presented as follows:

(1) Construct the finite element analysis of the cell in ANSYS 15.0 as the procedures presented in Section 3.1.

(2) Apply six (3D) nodal displacement fields $\chi^{0(\lambda\mu)}$ and $\chi^{*(\lambda\mu)}$ to each node, separately, and then run one static analysis for each nodal displacement field to obtain the corresponding nodal reaction force $f^{\lambda\mu}$ and $f^{*\lambda\mu}$. The applied nodal displacement fields are defined as:

$$\begin{aligned}
\chi_{node} &= \begin{pmatrix} u \\ v \\ w \\ \theta_x \\ \theta_y \\ \theta_z \end{pmatrix}, \quad \chi_{node}^{0(11)} = \begin{pmatrix} x \\ 0 \\ 0 \\ 0 \\ 0 \\ 0 \end{pmatrix}, \quad \chi_{node}^{0(22)} = \begin{pmatrix} 0 \\ y \\ 0 \\ 0 \\ 0 \\ 0 \end{pmatrix}, \quad \chi_{node}^{0(12)} = \begin{pmatrix} y/2 \\ x/2 \\ 0 \\ 0 \\ 0 \\ 0 \end{pmatrix}, \\
\chi_{node}^* &= \begin{pmatrix} u \\ v \\ w \\ \theta_x \\ \theta_y \\ \theta_z \end{pmatrix}, \quad \chi_{node}^{*(11)} = \begin{pmatrix} 0 \\ 0 \\ -x^2/2 \\ 0 \\ x \\ 0 \end{pmatrix}, \quad \chi_{node}^{*(22)} = \begin{pmatrix} 0 \\ 0 \\ -y^2/2 \\ y \\ 0 \\ 0 \end{pmatrix}, \quad \chi_{node}^{*(12)} = \begin{pmatrix} 0 \\ 0 \\ -xy/2 \\ -x/2 \\ y/2 \\ 0 \end{pmatrix}.
\end{aligned} \tag{7}$$

where (u, v, w) and $(\theta_x, \theta_y, \theta_z)$ are respectively the translational and rotational displacements of the shell element used in the finite element model, respectively.

(3) Apply the six nodal reaction forces $\mathbf{f}^{\lambda\mu}$ and $\mathbf{f}^{*\lambda\mu}$ to each node in the finite element model with periodic boundary conditions, separately. Subsequently, run one static analysis for each nodal reaction force to obtain the characteristic displacement field $\tilde{\mathbf{a}}^{\lambda\mu}$ and $\tilde{\mathbf{a}}^{*\lambda\mu}$. Note, the cell is periodic in in-plane and the boundary conditions for top and bottom faces are free.

(4) Apply the six characteristic displacement field $\tilde{\mathbf{a}}^{\lambda\mu}$ and $\tilde{\mathbf{a}}^{*\lambda\mu}$ to each node, and then run a static analysis to obtain the corresponding nodal reaction forces $\mathbf{p}^{\lambda\mu}$ and $\mathbf{p}^{*\lambda\mu}$.

(5) Calculate the effective stiffness moduli $\langle b_{\beta\zeta}^{\lambda\mu} \rangle$, $\langle b_{\beta\zeta}^{*\lambda\mu} \rangle = \langle z b_{\lambda\mu}^{\beta\zeta} \rangle$ and $\langle z b_{\beta\zeta}^{*\lambda\mu} \rangle$ from asymptotic homogenization formulas as given by:

$$\begin{aligned}
\langle b_{\beta\zeta}^{\lambda\mu} \rangle &= \frac{1}{|\Omega|} (\chi^{0(\beta\zeta)} - \tilde{\mathbf{a}}^{\beta\zeta})^T (\mathbf{f}^{\lambda\mu} - \mathbf{P}^{\lambda\mu}) \\
\langle b_{\beta\zeta}^{*\lambda\mu} \rangle &= \langle z b_{\lambda\mu}^{\beta\zeta} \rangle = \frac{1}{|\Omega|} (\chi^{0(\beta\zeta)} - \tilde{\mathbf{a}}^{\beta\zeta})^T (\mathbf{f}^{*\lambda\mu} - \mathbf{P}^{*\lambda\mu}) \\
\langle z b_{\beta\zeta}^{*\lambda\mu} \rangle &= \frac{1}{|\Omega|} (\chi^{*(\beta\zeta)} - \tilde{\mathbf{a}}^{*\beta\zeta})^T (\mathbf{f}^{*\lambda\mu} - \mathbf{P}^{*\lambda\mu})
\end{aligned} \tag{8}$$

in which $|\Omega| = L^2$ is the cell projected area for 2D periodic materials, and the complete expression of equivalent generalized stiffness matrix $\tilde{\mathbf{K}}$ is given as:

$$\begin{pmatrix} N_x \\ N_y \\ N_{xy} \\ M_x \\ M_y \\ M_{xy} \end{pmatrix} = \begin{pmatrix} \delta \langle b_{11}^{11} \rangle & \delta \langle b_{11}^{22} \rangle & \delta \langle b_{11}^{12} \rangle & \delta^2 \langle z b_{11}^{11} \rangle & \delta^2 \langle z b_{11}^{22} \rangle & \delta^2 \langle z b_{11}^{12} \rangle \\ \delta \langle b_{11}^{22} \rangle & \delta \langle b_{22}^{22} \rangle & \delta \langle b_{22}^{11} \rangle & \delta^2 \langle z b_{11}^{22} \rangle & \delta^2 \langle z b_{22}^{22} \rangle & \delta^2 \langle z b_{22}^{12} \rangle \\ \delta \langle b_{11}^{12} \rangle & \delta \langle b_{22}^{12} \rangle & \delta \langle b_{12}^{12} \rangle & \delta^2 \langle z b_{11}^{12} \rangle & \delta^2 \langle z b_{22}^{12} \rangle & \delta^2 \langle z b_{12}^{12} \rangle \\ \delta^2 \langle b_{11}^{*11} \rangle & \delta^2 \langle b_{11}^{*22} \rangle & \delta^2 \langle b_{11}^{*12} \rangle & \delta^3 \langle z b_{11}^{*11} \rangle & \delta^3 \langle z b_{11}^{*22} \rangle & \delta^3 \langle z b_{11}^{*12} \rangle \\ \delta^2 \langle b_{11}^{*22} \rangle & \delta^2 \langle b_{22}^{*22} \rangle & \delta^2 \langle b_{22}^{*12} \rangle & \delta^3 \langle z b_{11}^{*22} \rangle & \delta^3 \langle z b_{22}^{*22} \rangle & \delta^3 \langle z b_{22}^{*12} \rangle \\ \delta^2 \langle b_{11}^{*12} \rangle & \delta^2 \langle b_{22}^{*12} \rangle & \delta^2 \langle b_{11}^{*12} \rangle & \delta^3 \langle z b_{11}^{*12} \rangle & \delta^3 \langle z b_{22}^{*12} \rangle & \delta^3 \langle z b_{12}^{*12} \rangle \end{pmatrix} \begin{pmatrix} \varepsilon_x \\ \varepsilon_y \\ \gamma_{xy} \\ \kappa_x \\ \kappa_y \\ \kappa_{xy} \end{pmatrix} \tag{9}$$

where $(N_x, N_y, N_{xy}, M_x, M_y, M_{xy})$ are the stress resultants and bending moments; $(\varepsilon_x, \varepsilon_y, \gamma_{xy}, \kappa_x, \kappa_y, \kappa_{xy})$ are the strain, curvature and torsion; δ is the characteristic parameter of periodic cell and the value of δ is set as 1 herein. According to the NIAH, the equivalent stiffness matrix $\tilde{\mathbf{K}}$ for the present dual-constituent cell is obtained and expressed as:

$$\begin{pmatrix} A_{11} & A_{12} & 0 & B_{11} & B_{12} & 0 \\ A_{12} & A_{22} & 0 & B_{12} & B_{22} & 0 \\ 0 & 0 & A_{66} & 0 & 0 & B_{66} \\ B_{11} & B_{12} & 0 & D_{11} & D_{12} & 0 \\ B_{12} & B_{22} & 0 & D_{12} & D_{22} & 0 \\ 0 & 0 & B_{66} & 0 & 0 & D_{66} \end{pmatrix} \quad (10)$$

Note some coupling terms in $\tilde{\mathbf{K}}$ are very small, and thus can be considered as 0. The generalized stiffness matrix coefficient A_{11} is selected as the main evaluation indices to evaluate the equivalent stiffness of all feasible ZTE cell designs.

4. Results and discussion

In this section, the numerical results of the CTEs and the equivalent stiffness coefficients for various cell designs are obtained for parametric study and cell design evaluation. The main concerned points in this study are the cell equivalent stiffness and the thermal deformation control efficiency. The cell design evaluation will be carried out in terms of the curved surface design, patch covering form, patch shape and size.

4.1 The evaluation on the curved surface design

The evaluation on the curved surface design is first performed. With the assumption that the thicknesses of both curved surface and patch are kept constant, the CTEs α of the cells (a) and (d) are determined and presented in Fig.5(a)-(b), respectively. The x axis denotes the volume ratio V_0 / V and the cases with different curved surface angles θ are taken for comparison. As shown in Fig.5(a), the value of α decreases gradually with the increase of V_0 / V at the beginning, and this decreasing is mainly attributed to the enhanced effect of thermal bending-adjustment mechanism driven by the larger patch size. However, with the continuous increasing of V_0 / V , the α starts to increase. As such, it seems that the thermal bending-adjustment mechanism lost its effect. Actually, the final cell α is decided through the competition between the thermal bending-contraction and the extra thermal expansion driven by the patch. When the selected patch is oversized, the in-plane bending-contraction is hardly enough to compensate overall cell thermal expansion and consequently results in the increase of α . On

the other hand, the increased θ reinforces the effect of thermal bending-adjustment mechanism, and as a direct result, the α decreases monotonically. It can be also noticed from Fig.5(a) that the α of some cases decrease from positive to negative, and zero CTEs can be easily obtained if the appropriate design parameters are used. In addition, some cases such as $\theta = \pi / 70$ are unable to achieve the desired zero thermal expansion due to an excessive small θ that leads to insufficient in-plane contractions. Thus, it is necessary to delimit the curvature design range to promise the realization of in-plane ZTE.

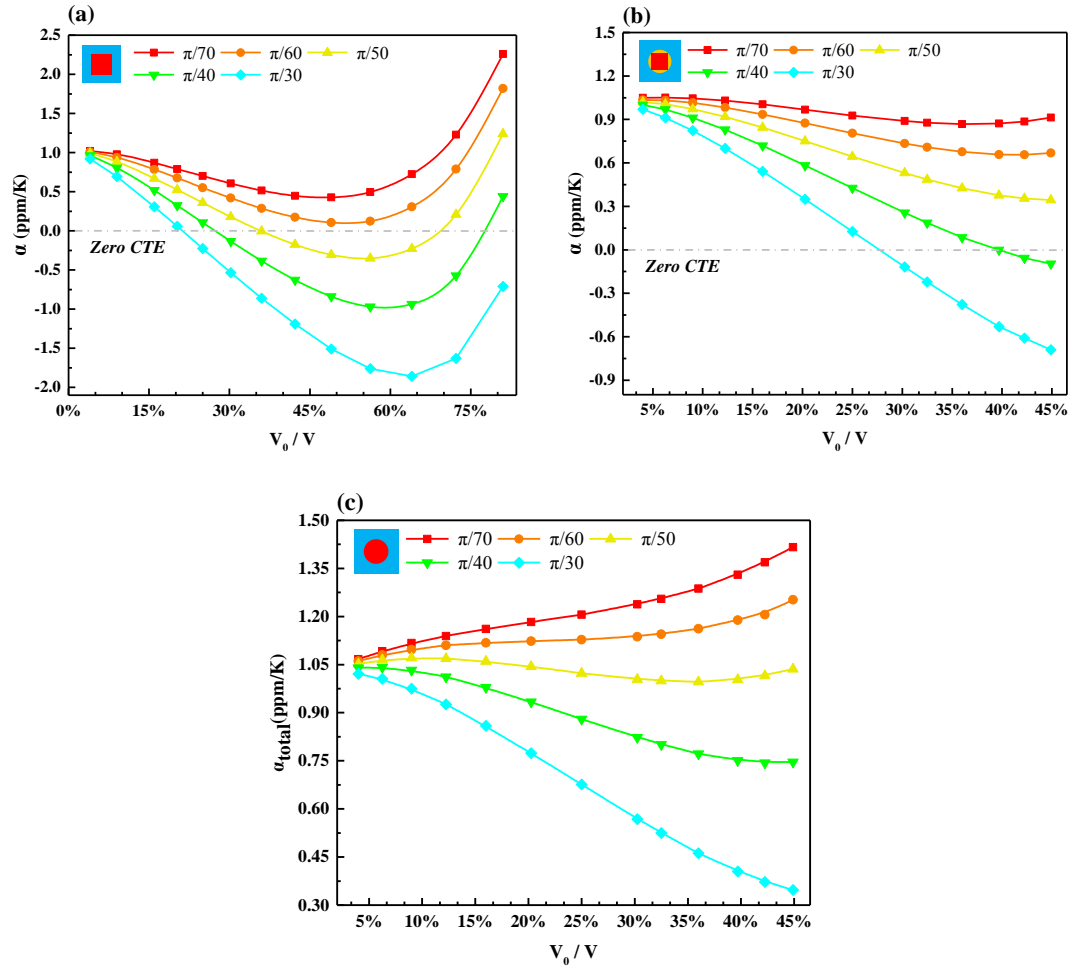


Fig.5. The CTEs α of dual-constituent cells with different volume ratio V_0/V and included angle θ . (a) Results for cell(a). (b) Results for cell(d). (c) Results for cell(e).

Fig.5(b) depicts α variation with the increasing of V_0/V for cell(d), and the decreased trend of α is relatively slow than that of cell(a) within V_0/V range of 4.00%–44.89%. The reason is attributed to the poor thermal deformation control of Type B curved surface, which enables the cell(d) without providing strong bending-contraction for compensating in-plane thermal expansion. Moreover, this conclusion can be further proved through presenting the results

of cell(e). In Fig.5(c), the efficiency of thermal deformation control of cell(e) is the worst, and the expected decrease in α never show up even for the cases with smaller θ . Consequently, the cell(e) with type B curved surface and circle-shaped patch is unable to obtain feasible ZTE design within all possible selections of parameters. Additionally, the circle projected area of Type B curved surface limits the maximum patch size, which leads to narrow patch design areas for producing further in-plane contraction.

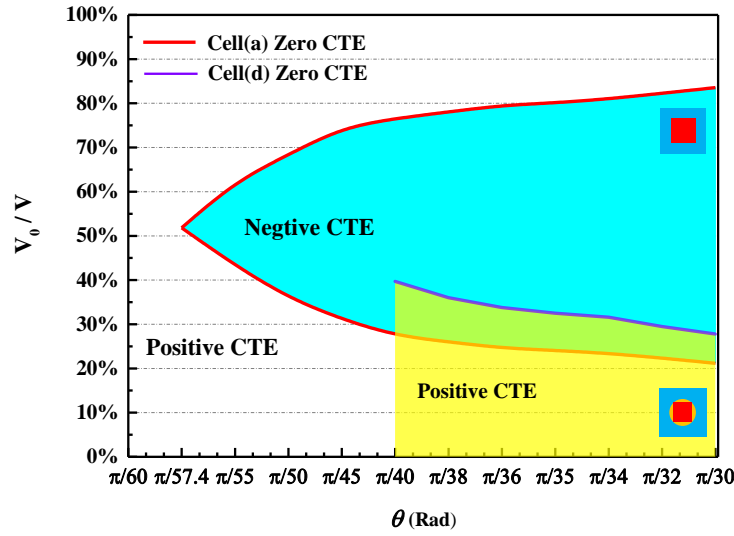


Fig.6. The feasible designs of zero thermal expansion for cell(a) and (d).

In order to obtain a clear comparison on thermal deformation control between cells(a) and (d), the feasible ZTE designs and corresponding design parameters are plotted in Fig.6. As shown in Fig.6, except for the case of $\theta = \pi / 57.4$, the cell(a) with Type A curved surface has two sets of ZTE designs for each curved surface angle θ , whereas the cell(d) has the only one. Furthermore, compared with the cell(d), the cell(a) possesses broader curvature design range of $\pi / 57.4 - \pi / 30$. It requires smaller patch volume for obtaining in-plane ZTE as selecting the first ZTE design with small V_0/V . More importantly, the obvious differences between the results of two cell designs prove that the curved surface design produces non-negligible influences on thermal deformation control and the Type A curved surface with better thermal deformation control performance is appropriate for the implementation of the present cell design for achieving desired in-plane ZTE.

4.2 The evaluation on the patch covering form and shape design

Besides the curved surface, the configuration of patch including patch covering form and shape is another important design aspect for the efficiency of cell thermal deformation control. To this end, the cells(a)-(c) with sharing the same Type A curved surface and different patch configurations are taken as an example for comparative analysis. The CTEs variation with the increasing of V_0/V for all selected cells are separately shown in Fig.7(a)-(c), which gives a consistent variation trend on α and similar thermal deformation tuning range. Furthermore, with adopting the same curved surface angle θ , the cell(c) with cross-shaped patch required a relative small patch volume than any other two cells. In order to further clarify this conclusion, all of the feasible designs that achieve the in-plane ZTE of the cells(a)-(c) is plotted in Fig.8.

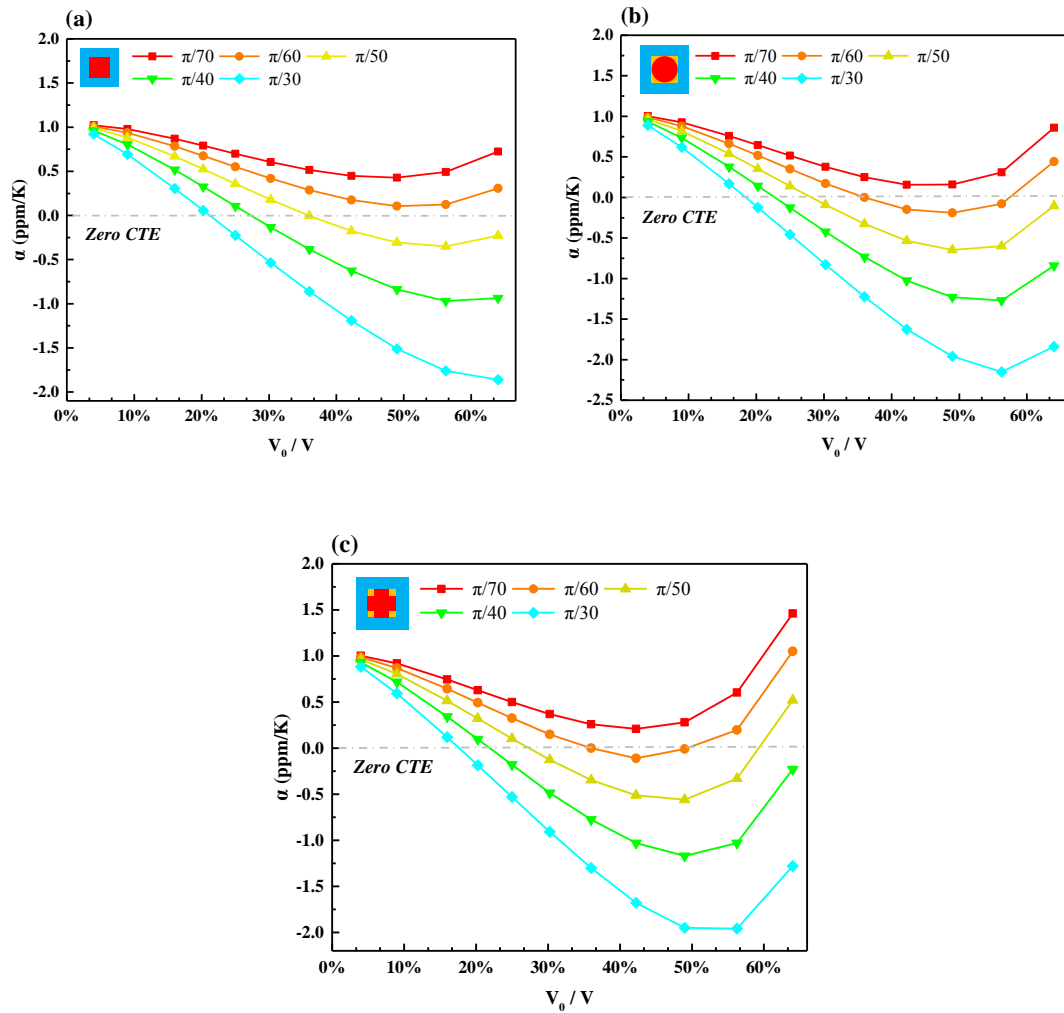


Fig.7. The CTEs α of dual-constituent cells with different volume ratio V_0/V and included angle θ . (a) Results for cell(a). (b) Results for cell(b). (c) Results for cell(c).

From Fig.8, it can be seen that the cells(a)-(c) with specific θ generally corresponds to two sets of design parameters for in-plane ZTE. For the first ZTE designs with small V_0/V , the patch volume decreases with the increasing of θ , while the other ZTE designs with large V_0/V shows an opposite trend. On the other hand, the patch configuration exhibits significant influences on cell ZTE design. Clearly, the cells(b) and (c) with partially covered patch on central area A possess broader curvature design range and require relatively low V_0/V than that of cell(a) with completely covered patch. However, it seems that the shape of the patch has a little effect on cell ZTE design, which can be concluded from the consistent curvature design range and similar ZTE design parameters for cells(b) and (c) presented in Fig.8.

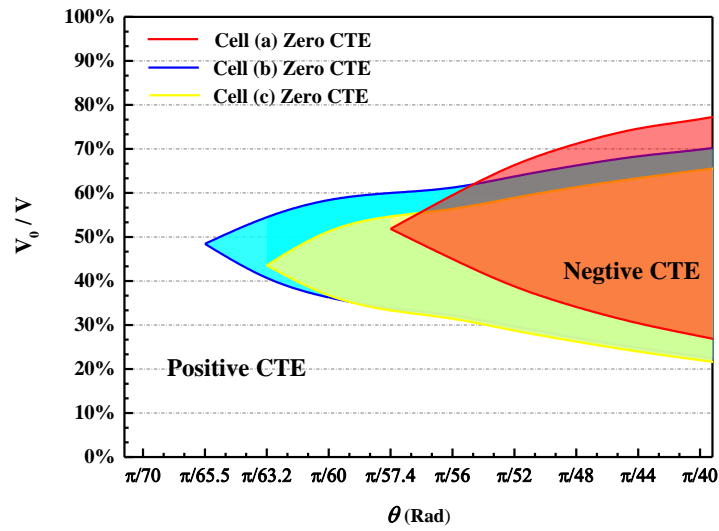


Fig.8. The feasible designs with achieving in-plane ZTE for cells (a)-(c).

As the in-plane ZTE is achieved, the equivalent stiffness to be another evaluation aspect used for filtering all the feasible cell designs. Thus, the NIAH presented in Section 3.2 for predicting cell stiffness is adopted, and the generalized stiffness matrix coefficient \tilde{A}_{11} is taken as mainly evaluation index in comparative analysis. The stiffness coefficients \tilde{A}_{11} of the two sets of ZTE designs as given in Fig.8 are plotted in Fig.9(a)-(c), respectively. Obviously the cells(a)-(c) give the consistent trend that the \tilde{A}_{11} of the first ZTE designs with small V_0/V increase with increasing of the θ at the beginning, and then turn to decrease. In addition, for the second ZTE designs with large V_0/V , the \tilde{A}_{11} decrease monotonously with the increase of θ , and the results are all smaller than those of the first ZTE designs under the same conditions. Therefore, there exists a local maximum value of \tilde{A}_{11} and the desired optimal designs with a combination of in-plane ZTE and high stiffness for every cell type could be found. Furthermore, compared with

cells(b) and (c), the cells(a) with completely covered patch and $\theta = \pi / 45$ possesses global maximum \tilde{A}_{11} than any other designs presented in Fig.9(a)-(c).

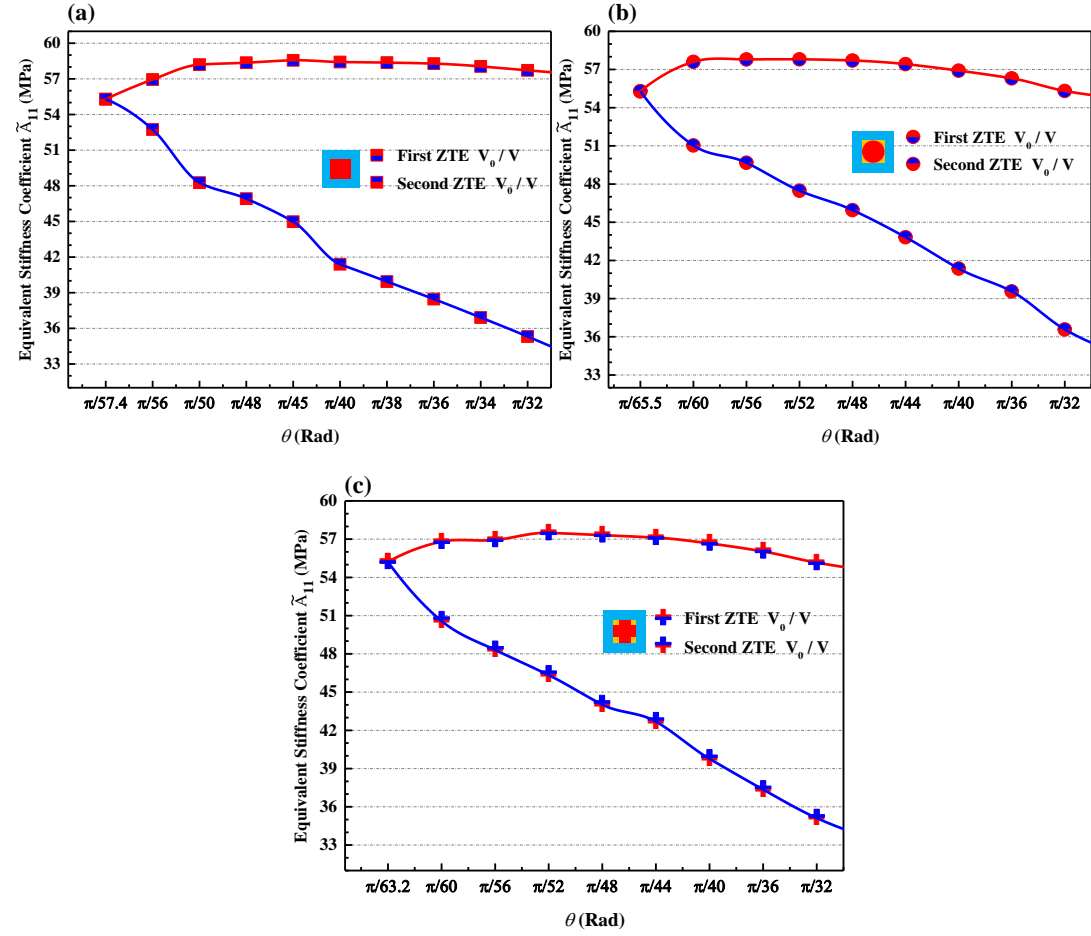


Fig.9. The generalized stiffness matrix coefficients A_{11} for all selected cells. (a) Results for cell(a). (b) Results for cell(b). (c) Results for cell(c).

However, the designs for higher stiffness will require much larger patch size than those designs with lower stiffness, such as the case of cell(b) with $\theta = \pi / 56$ and $\theta = \pi / 30$. Hence, another evaluation index of ratio of coefficient \tilde{A}_{11} to total cell mass M is subsequently introduced to comprehensively evaluate the cell design through combining the stiffness and weight. It should be mentioned that the discussions on the second ZTE designs are meaningless due to a lower equivalent stiffness and accompanying larger patch volume. As shown in Fig.10, with the increasing of θ , the \tilde{A}_{11} / M for cells(a)-(c) are first increased and then decreased, and the global maximum \tilde{A}_{11} / M correspond to the cell design of square-shaped patch and $\theta = \pi / 36$. Therefore, it is easily concluded that at present the optimal design is the cell(a) with

square-shaped patch and the curved surface $\theta = \pi / 36$, and as the desired in-plane ZTE is achieved, the completely covering form of patch results in higher cell stiffness and lighter weight.

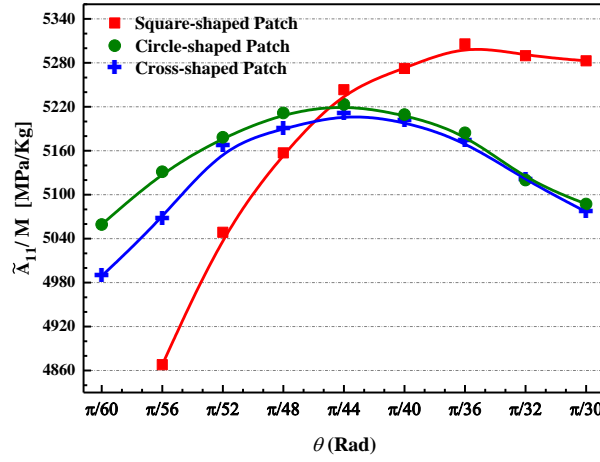


Fig.10. The comparison of evaluation index \tilde{A}_{11} / M for cells(a)-(c) with different patch shapes.

4.3 The influences of patch thickness on dual-constituent cell design

In the above numerical analysis, the influences of patch thickness variation on cell thermal expansion characteristic and stiffness are not considered. In fact, this design aspect is very important and hardly to be avoided for the dual-constituent cell design that is required to achieve the high cell stiffness and in-plane ZTE, simultaneously. Therefore, as for the cell with various patch thickness, the patch volumes are needed for achieving the in-plane ZTE in Fig.11(a), and the stiffness coefficient \tilde{A}_{11} is plotted in Fig.11(b). The cell(a) with square-shaped patch is taken as the sole research objective due to the best mechanical performance has been proved in Section 4.2. Additionally, the four kinds of θ including the optimal stiffness design parameter of $\theta = \pi / 36$ are presented for comparison study.

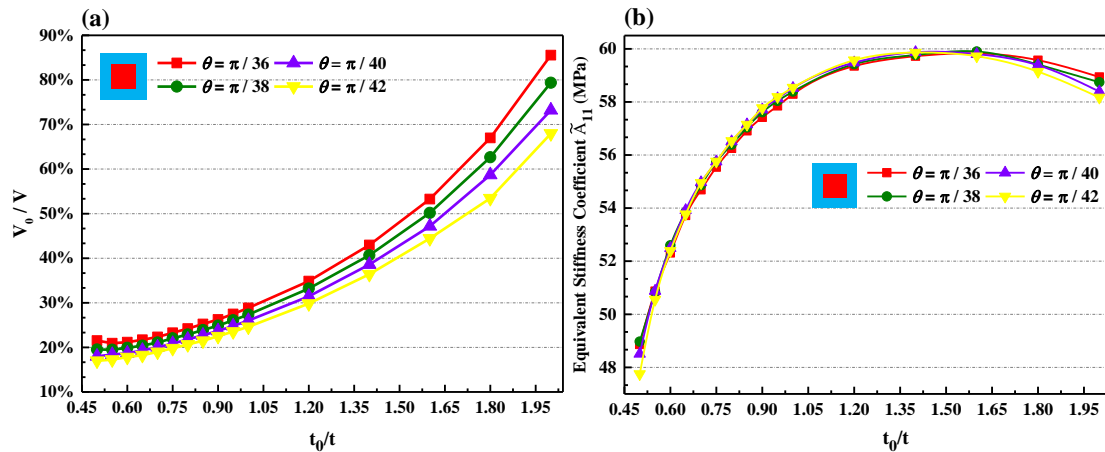


Fig.11. The influences of patch thickness on face sheet cell design. (a) The patch volume needed for in-plane ZTE. (b) The influence of patch thickness on cell stiffness.

As shown in Fig.11(a), the patch volumes that are needed for achieving in-plane ZTE attributes increase monotonically. The dual-constituent cells tend to become low efficiency on thermal deformation control when the patch thickness is getting thicker. In Fig.11(b), the stiffness coefficients \tilde{A}_{11} for all cases with different θ are increased firstly and then decreased along with the increasing of the patch thickness, and the optimal cell stiffness corresponds to the design parameters of $\theta = \pi/36$ and $t_0/t = 1.6$. It should be mentioned that the design on patch thickness is limited by various factors such as manufacturing technology and engineering requirements, and the patch thickness keeping within the twice thickness of curved surface is plausible in practical.

Additionally, the comprehensive evaluation with combination of stiffness and weight is also performed for patch thickness design. As shown in Fig.12(a), the evaluation index \tilde{A}_{11}/M increases non-monotonically with the increasing of patch thickness, and the patch designs with approximate once curved surface thickness gives higher cell stiffness and lighter weight. On the other hand, the stiffness reduction factor of dual-constituent cell is also calculated through introducing the ratio of \tilde{A}_{11} to the corresponding stiffness coefficient A_{11} of flat panel in same geometric size, and the latter can be obtained by the analytical formula of $A_{11} = Et/(1-\nu^2)$. As shown in Fig. 12(b), the stiffness reduction factor \tilde{A}_{11}/A_{11} increases with the increasing of the patch thickness at the beginning, and subsequently starts to decrease. The maximum stiffness reduction factor for cells(a) is about 0.79, which means acceptable stiffness loss and sufficient residual stiffness for load-carrying as desired in-plane ZTE characteristic is achieved.

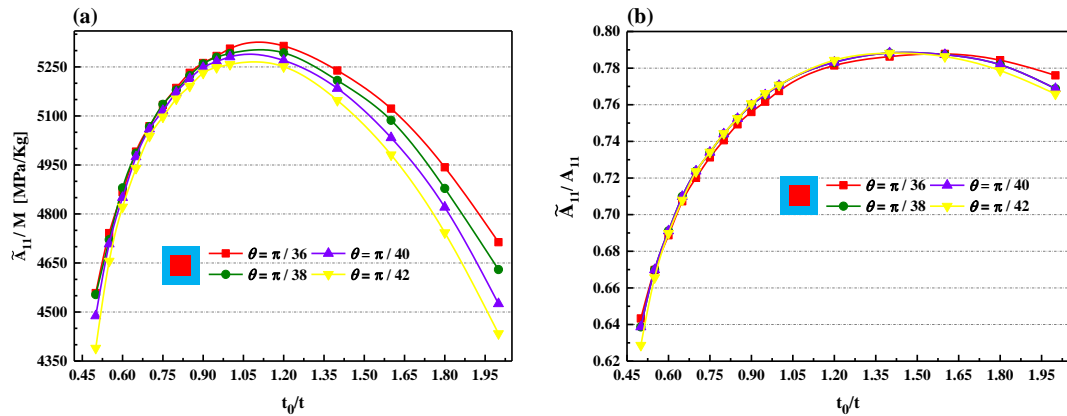


Fig.12. The influences of patch thickness on face sheet cell design. (a) The influence of patch thickness on evaluation index \tilde{A}_{11} / M . (b) The stiffness reduction factor \tilde{A}_{11} / A_{11} of face sheet cell with various patch thickness.

5. Conclusion

In this paper, a novel dual-constituent lattice sandwich panel with desired in-plane ZTE and surface imporous attribute is designed and analyzed. The detailed designs on basic face sheet cells for achieving the in-plane ZTE and high stiffness, simultaneously, are carried out. Six kinds of cell designs through combining two types of curved surface and various patch configurations are devised. The optimal ZTE cell design with high special stiffness is finally obtained through a serious of comparative analyses. Finally, the main design principles for guiding imporous in-plane ZTE panel design within present patch method are revealed, and the main conclusive points are summarized as follows:

- (1) The design of cell curved surface could prominently improve the control efficiency of the face sheet thermal deformation, and a better design of curved surface requires less patch material for achieving the desired in-plane ZTE attribute.
- (2) The size of curved surface angle and patch needed for tailoring cell CTEs should be well designed. Adopting excessive small curved surface angle or oversized patch may lead to cell insufficient in-plane contractions, and as a consequence, it inevitably fails in obtaining cell in-plane ZTE.
- (3) The patch configuration has significant influences on cell ZTE design. The cells with partially covered patch possess broader ZTE curvature design range and require relatively less patch material. However, the completely covering form of patch shows better mechanical performance of higher cell stiffness and lighter weight.
- (4) The patch thickness design could further improve maximum cell stiffness. Theoretically, the patch design with approximate once curved surface thickness possesses higher cell stiffness and lighter weight, simultaneously.
- (5) Compared with completely flat dual-constituent cell, the stiffness reduction of present cell design for in-plane ZTE is acceptable. The approximate 80% residual cell stiffness ensures the dual-constituent lattice sandwich panel possessing sufficient load carrying capacity.

Acknowledgements

The work is supported by National Science Foundation of China (Grant no. 11572071,

U1808215), Program for Changjiang Scholars and Innovative Research Team in University (PCSIRT), 111 Project (B14013). We would also like to thank the Fundamental Research Funds for the Central Universities (DUT19GF102).

References:

- [1]. Shi, S., C. Dai and Y. Wang. Design and optimization of an integrated thermal protection system for space vehicles. in Aiaa International Space Planes and Hypersonic Systems and Technologies Conference. 2015.
- [2]. Chen, P., et al. Aerothermodynamic Optimization of Hypersonic Vehicle TPS Design by POD/RSM-Based Approach. in Aiaa Aerospace Sciences Meeting and Exhibit. 2006.
- [3]. Du, Z., et al., Design and application of composite platform with extreme low thermal deformation for satellite. *Composite Structures*, 2016. 152: p. 693-703.
- [4]. Wang, B., J. Yan and G. Cheng, Optimal structure design with low thermal directional expansion and high stiffness. *Engineering Optimization*, 2011. 43(6): p. 581-595.
- [5]. Wakashima, K., T. Suganuma and T. Ito, Use of glass fibers in tailoring laminated composites with directionally negative and near-zero coefficients of thermal expansion. *Advanced Composite Materials*, 2001. 10(4): p. 329-338.
- [6]. Liu, Q.Q., X.N. Cheng and J. Yang, Development of low thermal expansion $\text{Sc}_2(\text{WO}_4)_3$ containing composites. *Materials & Processing Report*, 1996. 27(5): p. 388-392.
- [7]. Cribb, J.L., Shrinkage and Thermal Expansion of a Two Phase Material. *Nature*, 1968. 220(5167): p. 576-577.
- [8]. Lehman, J. and R. Lakes, Stiff lattices with zero thermal expansion. *Journal of Intelligent Material Systems & Structures*, 2012. 23(23): p. 1263-1268.
- [9]. Lehman and Jeremy, Stiff lattices with zero thermal expansion and enhanced stiffness via;rib cross section optimization. *International Journal of Mechanics & Materials in Design*, 2013. 9(3): p. 213-225.
- [10]. Sigmund, O. and S. Torquato, Design of materials with extreme thermal expansion using a three-phase topology optimization method. *Proceedings of SPIE - The International Society for Optical Engineering*, 1997. 45(6): p. 1037-1067.
- [11]. Sigmund, O. and S. Torquato, Composites with Extremal Thermal Expansion Coefficients. *Applied Physics Letters*, 1996. 69(21): p. 3203-3205.
- [12]. Steeves, C.A., et al., Experimental investigation of the thermal properties of tailored expansion lattices. *International Journal of Mechanics & Materials in Design*, 2009. 5(2): p. 195-202.
- [13]. Steeves, C.A., et al., Concepts for structurally robust materials that combine low thermal expansion with high stiffness. *Journal of the Mechanics & Physics of Solids*, 2007. 55(9): p. 1803-1822.
- [14]. Wei, K., et al., Tailorable Thermal Expansion of Lightweight and Robust Dual-Constituent Triangular Lattice Material. *Journal of Applied Mechanics*, 2017. 84(10): p. 101006-101006-9.
- [15]. Wei, K., et al., A cellular metastructure incorporating coupled negative thermal expansion and negative Poisson's ratio. *International Journal of Solids & Structures*, 2018.
- [16]. Xu, H., A. Farag and D. Pasini, Multilevel hierarchy in bi-material lattices with high specific stiffness and unbounded thermal expansion. *Acta Materialia*, 2017. 134.

- [17]. Xu, H. and D. Pasini, Structurally Efficient Three-dimensional Metamaterials with Controllable Thermal Expansion. *Scientific Reports*, 2016. 6: p. 34924.
- [18]. Zhang, Y.C., et al., A new design of dual-constituent triangular lattice metamaterial with unbounded thermal expansion. *Acta Mechanica Sinica*, 2018.
- [19]. Yongcun, Z.A.Y.L., A new design for enhanced stiffness of dual-constituent triangular lattice metamaterial with unbounded thermal expansion. *Materials Research Express*, 2019. 6(1): p. 015705.
- [20]. Steeves, C.A., et al. Design of a Robust, Multifunctional Thermal Protection System Incorporating Zero Expansion Lattices. in *ASME 2007 International Mechanical Engineering Congress and Exposition*. 2007.
- [21]. Wei, K., et al., Design and analysis of lattice cylindrical shells with tailorable axial and radial thermal expansion. *Extreme Mechanics Letters*, 2018. 20.
- [22]. Wei, K., et al., Three dimensional lightweight lattice structures with large positive, zero and negative thermal expansion. *Composite Structures*, 2018. 188.
- [23]. Zhang, Y.C., et al., A new design concept of dual-constituent sandwich panel with in-plane zero thermal expansion. *Smart Materials and Structures* (Accept).
- [24]. Lehman, J. and R. Lakes, Stiff, strong zero thermal expansion lattices via the Poisson effect. *Journal of Materials Research*, 2013. 28(17): p. 2499-2508.
- [25]. Cai, Y., L. Xu and G. Cheng, Novel numerical implementation of asymptotic homogenization method for periodic plate structures. *International Journal of Solids & Structures*, 2014. 51(1): p. 284-292.